

Featuring work from Professor Stuart Ibsen's research team which focuses on the development of new liquid biopsy techniques using label-free dielectrophoresis particle collection technology for early-stage cancer detection, at the Department of Biomedical Engineering and The Knight Cancer Institute's Cancer Early Detection Advanced Research Center, Oregon Health and Science University, USA.

Automated fluorescence quantification of extracellular vesicles collected from blood plasma using dielectrophoresis

The authors designed an automated algorithm and an internal standard to quantify the fluorescent signal of immunolabeled biological nanoparticles, which were collected at predictable locations within a microfluidic device. Here, dielectrophoretic forces concentrated extracellular vesicles around the edges of circular electrodes on a microfluidic chip from undiluted plasma. Collection regions were automatically identified, background noise levels were defined (shown by the black squares), and background was subtracted from fluorescent signal (columns). The internal standard particles, spiked with known concentration into the sample, were collected simultaneously with biological nanoparticles enabling direct comparison between samples.

### As featured in:



See Stuart D. Ibsen *et al.*,  
*Lab Chip*, 2021, 21, 1318.


 Cite this: *Lab Chip*, 2021, 21, 1318

## Automated fluorescence quantification of extracellular vesicles collected from blood plasma using dielectrophoresis†

 Kyle T. Gustafson,<sup>iD</sup><sup>ab</sup> Katherine T. Huynh,<sup>iD</sup><sup>ab</sup> Daniel Heineck,<sup>ab</sup> Jesus Bueno,<sup>ab</sup> Augusta Modestino,<sup>ab</sup> Sejung Kim,<sup>iD</sup><sup>ab</sup> Austin Gower,<sup>a</sup> Randall Armstrong,<sup>a</sup> Carolyn E. Schutt<sup>ab</sup> and Stuart D. Ibsen<sup>iD</sup><sup>\*ab</sup>

Tumor-secreted exosomes and other extracellular vesicles (EVs) in circulation contain valuable biomarkers for early cancer detection and screening. We have previously demonstrated collection of cancer-derived nanoparticles (NPs) directly from whole blood and plasma with a chip-based technique that uses a microelectrode array to generate dielectrophoretic (DEP) forces. This technique enables direct recovery of NPs from whole blood and plasma. The biomarker payloads associated with collected particles can be detected and quantified with immunostaining. Accurately separating the fluorescence intensity of stained biomarkers from background (BG) levels becomes a challenge when analyzing the blood from early-stage cancer patients in which biomarker concentrations are low. To address this challenge, we developed two complementary techniques to standardize the quantification of fluorescently immunolabeled biomarkers collected and concentrated at predictable locations within microfluidic chips. The first technique was an automated algorithm for the quantitative analysis of fluorescence intensity at collection regions within the chip compared to levels at adjacent regions. The algorithm used predictable locations of particle collection within the chip geometry to differentiate regions of collection and BG. We successfully automated the identification and removal of optical artifacts from quantitative calculations. We demonstrated that the automated system performs nearly the same as a human user following a standard protocol for manual artifact removal with Pearson's *r*-values of 0.999 and 0.998 for two different biomarkers (*n* = 36 patients). We defined a usable dynamic range of fluorescence intensities corresponding to 1 to 2000 arbitrary units (a.u.). Fluorescence intensities within the dynamic range increased linearly with respect to exposure time and particle concentration. The second technique was the implementation of an internal standard to adjust levels of biomarker fluorescence based on the relative collection efficiency of the chip. Use of the internal standard reduced variability in measured biomarker levels due to differences in chip-to-chip collection efficiency, especially at low biomarker concentrations. The internal standard did not affect linear trends between fluorescence intensity and exposure time. Adjustments using the internal standard improved linear trends between fluorescence intensity and particle concentration. The optical quantification techniques described in this paper can be easily adapted for other lab-on-a-chip platforms that have predefined regions of biomarker or particle collection and that rely on fluorescence detection.

 Received 16th September 2020,  
 Accepted 27th February 2021

DOI: 10.1039/d0lc00940g

[rsc.li/loc](http://rsc.li/loc)

<sup>a</sup> Cancer Early Detection Advanced Research Center, Knight Cancer Institute, Oregon Health & Science University, USA. E-mail: [ibsen@ohsu.edu](mailto:ibsen@ohsu.edu)

<sup>b</sup> Department of Biomedical Engineering, School of Medicine, Oregon Health & Science University, USA

† Electronic supplementary information (ESI) available: A technical flow diagram describes the design sequence of the algorithm to quantify fluorescence images. Histograms of pixel intensities in the ROI and BG of three representative electrodes show collection below, within, and above the detection limits set by the usable dynamic range. Size distribution data show the selection of a subpopulation of HeLa-derived EVs that coincides with the accepted size range of exosomes. Fluorescence images were exported using described parameters into a specific file structure for automated analysis. The algorithm for automated fluorescence quantification is included in its entirety as MATLAB® code. See DOI: 10.1039/d0lc00940g

## 1. Introduction

Tumors release various types of cancer-related biomarkers into circulation starting from early stages and continuing throughout their development.<sup>1–4</sup> Liquid biopsy techniques are designed to detect these biomarkers (e.g. including DNA, RNA, and proteins) in blood samples. Compared to invasive and localized tissue biopsies, liquid biopsies are advantageous as a cancer-screening tool. Blood collection is minimally invasive and offers the potential to detect biomarkers released across the entire tumor lesion, which can more accurately depict tumor heterogeneity.



Many cancer-specific biomarkers are associated with lipid-based nanoparticles (NPs) called extracellular vesicles (EVs), which are secreted by tumor cells<sup>5</sup> in elevated quantities. Exosomes are one type of EV that are difficult to recover from blood due to their small size (50 to 150 nm diameter)<sup>6–8</sup> and low buoyant density. Recovery of exosomes is a fundamental challenge for quantifying their associated biomarkers. Traditional “gold-standard” methods to recover exosomes for biomarker analysis include ultracentrifugation and filtration-based separations, which are time-consuming and labor-intensive.<sup>9–13</sup> New lab-on-a-chip systems for NP separation efficiently recover EVs from blood plasma.<sup>14–16</sup>

Dielectrophoresis (DEP) is the motion of an object due to dielectrophoretic forces. When an object suspended in fluid is subjected to a non-uniform electric field, contrasting dielectric properties of the object and its surrounding media induce DEP forces on the object. In particular, DEP<sup>17</sup> applied

to the microfluidic environment can preferentially concentrate tumor-derived NPs to known locations within the chip<sup>14–16</sup> as shown in Fig. 1. Blood-derived plasma samples are loaded into the microfluidic chamber on top of a planar microarray of circular electrodes. When an AC voltage is applied across electrodes, this particular microarray geometry creates a strong electric field gradient that exerts DEP forces on EVs and other endogenous NPs in the fluid sample. These NPs are collected at maxima in the electric field gradient known as “high-field” regions (Fig. 1a), which are located at the circumferences of each electrode in the planar microarray as predicted by theoretical simulations (Fig. 1d) and confirmed by scanning electron microscopy (Fig. 1g and h). NPs are held in place by positive DEP (pDEP) forces during washing, which removes the bulk plasma. Subsequent immunostaining and fluorescence imaging of the collected NPs enables detection and quantification of their associated

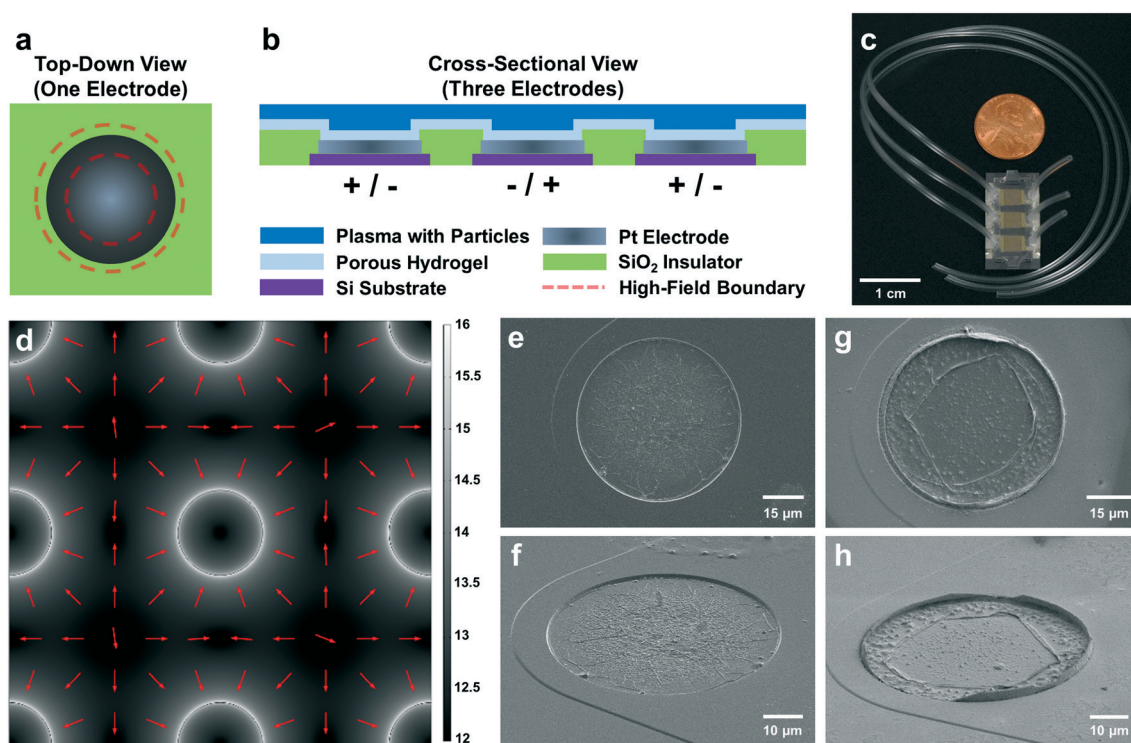


**Fig. 1** NPs were collected in the “high-field” regions around the electrode edges under pDEP: a) top-down view of a circular electrode in the planar microarray of a DEP chip. EVs and other NPs were collected at the electrode edge by DEP forces (area between dashed red lines). b) Cross-sectional area of three electrodes in the planar microarray of a DEP chip. A layer of silicon dioxide insulated platinum electrodes, which were patterned on top of a silicon substrate. A porous hydrogel layer on the surface of the chip separated electrodes from direct contact with blood-derived plasma. c) Tubing was inserted into three microfluidic chambers on a DEP chip to prepare the device for experimentation. Each microfluidic chamber housed thousands of microelectrodes. The DEP chip is shown beside a penny for scale. d) A simulation of the gradient of the square magnitude of the electric field demonstrated a pattern of high-field regions (white) and low-field regions (black). Numbers by the greyscale heat map indicated base-10 exponents spanning magnitudes of  $10^{12}$  to  $10^{16}$   $\text{V}^2 \text{m}^{-3}$ . NPs responsive to pDEP forces were predicted to move up the gradient along the direction of the red arrows from low- to high-field regions. High-field regions coincided with the circumferences of electrodes in the planar microarray. e and f) Respectively, scanning electron micrographs (SEMs) of a top-down view and an angled view (tilt angle =  $59^\circ$ ) show typical electrodes on a DEP chip after running DEP in a filtered  $0.5\times$  PBS buffer in the absence of added nanoparticles. The scale bar in panel e applies to the vertical and horizontal dimensions along the image plane, while the scale bar in panel f describes the horizontal dimension only. g and h) SEMs of top-down and angled views (tilt angle =  $59^\circ$ ) show typical electrodes on a DEP chip that was used to collect endogenous NPs from undiluted plasma. NPs were collected into a raised ridge structure at the outer edge of the electrode. This raised ridge was not observed in the buffer control shown in panels e and f. Collection at the electrode edge agrees with the simulation shown in panel d. The scale bar in panel g applies to the vertical and horizontal dimensions along the image plane, while the scale bar in panel h describes the horizontal dimension only.



biomarkers. The collection of endogenous NPs at the electrode circumferences increases their local concentration, and thereby the fluorescent signal, enhancing the signal-to-noise ratio (SNR).

Applying this DEP technique to early cancer detection presents a unique set of challenges stemming from characteristically low concentrations of biomarkers present in circulation at early stages of disease.<sup>18–20</sup> In order to address the challenge of inherently low SNRs, it is critical to measure the level of BG noise and to separate BG levels from the detected signal of immunofluorescently stained biomarkers. Here we demonstrate a custom optical imaging algorithm, written with MATLAB® software, to automate quantification for this type of immunofluorescent staining. The algorithm for fluorescence quantification described in this paper zeroes pixel intensities at each region of collection (“region-of-interest”, or “ROI”) to the noise level (*e.g.* average pixel intensity plus three standard deviations) of the local BG. Localized noise-subtraction treated collection at each ROI in a field-of-view as a unique sampling of biomarkers from the plasma. Localized comparisons were important because BG fluorescence can vary throughout a single field-of-view, across multiple fields-of-view on a single chip, and across multiple fields-of-view for different chips.

To address the challenge of inherently low levels of target biomarkers, it was also necessary to reduce user bias in quantitation. Biomarkers were collected at predictable ROIs, allowing for localized noise subtraction as previously mentioned. The ability to predict the locations of biomarker collection based on the geometry of the planar electrode microarray in the DEP chip also allowed us to automate quantitative calculations, including the removal of optical artifacts. Complete automation of quantitative calculations successfully minimized user bias in fluorescence analysis and reduced analysis time. Automated artifact removal performed as well as a single user following a controlled protocol for manual artifact removal.

We also developed an internal standard, consisting of a known concentration of fluorescent NPs, to correct for the variability in collection efficiency across DEP chips and to further address the challenge of low SNRs. Fluorescent NPs and target biomarkers were collected simultaneously and quantified using the custom algorithm. The internal standard ensured that observed differences in fluorescence intensity between two or more biological samples reflected physiological differences in endogenous biomarker levels rather than a discrepancy in collection efficiencies across DEP chips.

Many lab-on-a-chip designs focus on the separation and concentration of target particles into predictable locations. Other designs include implementations of DEP where exosomes,<sup>14,15</sup> stem cells,<sup>21,22</sup> blood cells,<sup>23,24</sup> cancer cells,<sup>25–27</sup> bacteria,<sup>28,29</sup> viruses,<sup>30,31</sup> and synthetic NPs<sup>16,32,33</sup> are all collected in predictable locations. Other collection modes include electrophoretic,<sup>34</sup> magnetophoretic,<sup>35,36</sup> and acoustophoretic<sup>37–39</sup> forces to concentrate targets from surrounding media to known regions on the chip. Several

devices utilize immunoaffinity capture of EVs either by functionalized NPs<sup>40</sup> or at patterned locations on the chip.<sup>41</sup> Still others use increased affinity for substrates coated in nanotubes to collect aberrant circulating tumor cells.<sup>42</sup> The automated algorithmic approach described here can be easily adapted for use with other chip geometries by changing the shape of the digital mask to encompass the ROI. Masking makes the algorithm a widely applicable tool to reduce user bias, labor, and time in analyzing large numbers of samples. Masking also reduces BG noise for more accurate quantification of low abundance targets.

## 2. Materials & methods

### 2.1 Particle collection using DEP for development of optical quantification algorithm

**2.1.1 Materials.** Monoclonal mouse anti-CD9 antibody conjugated to Alexa Fluor 488 was purchased from R&D Systems (Minneapolis, MN; FAB1880G; clone #209306). Monoclonal mouse anti-CD63 antibody conjugated to Alexa Fluor 647 was purchased from Novus Biologicals (Centennial, CO; NB10077913Y; clone MEM-259). FluoSpheres™ carboxylate-modified microspheres (0.1 μm, blue fluorescent 350/440, 2% solids; F8797) and D-(+)-trehalose dihydrate (Fisher BioReagents, BP2687100) were purchased from Thermo Fisher Scientific (Waltham, MA). Three-chamber DEP chips (EF-CRT-00002) were purchased from Biological Dynamics (San Diego, CA). Dulbecco’s modified Eagle’s medium (DMEM), fetal bovine serum (FBS), and penicillin-streptomycin (P/S) were purchased from Thermo Fisher Scientific (Waltham, MA). Amicon® Ultra-15 centrifugal filter units (25 mL, 100 kDa MWCO; UFC901024) and ultrafiltration membrane filter discs (10 kDa MWCO, BioMax; PBGC07610; and 300 kDa MWCO, BioMax; PBMK07610) were purchased from MilliporeSigma (Burlington, MA). Sterile filtration units (0.1 mM; Nalgene; 5670010) were purchased from Thermo Fisher Scientific (Waltham, MA). BD Difco™ skim milk was purchased from Midland Scientific (Omaha, NE; DIFCO 232100).

**2.1.2 Collection of EVs from HeLa cell culture media.** Exosome-depleted cell culture media was prepared to harvest EVs from HeLa cells. Exosome-depleted FBS was prepared by 300 kDa MWCO ultrafiltration with an Amicon stirred-cell concentrator followed by 0.1 μM filter sterilization. Filtered FBS was added to DMEM to a final concentration of 10% by volume. P/S was added to exosome-depleted media at a concentration of 1% by volume. Non-exosome-depleted cell culture media was prepared with commercial FBS and P/S at final concentrations of 10% and 1% by volume, respectively. Cells were cultured to approximately 50% confluency in non-exosome-depleted media. Media was discarded, and cells were washed with 1× phosphate-buffered saline (PBS). PBS was discarded, and cells incubated in exosome-depleted media for 48 hours. Exosome-depleted media was collected and cells were removed by centrifugation. D-Trehalose was



added to media at a final concentration of 25 mM to stabilize EVs during storage. Conditioned media was stored at  $-80\text{ }^{\circ}\text{C}$  until a total of approximately 1.5 L had been collected.

Conditioned media (1.5 L) was thawed and concentrated to approximately 20 mL using an Amicon stirred-cell concentration (10 kDa filter size). Concentrated media was centrifuged (30 minutes; 10 000g;  $4\text{ }^{\circ}\text{C}$ ) and protein aggregates were removed. EVs were then concentrated to approximately 5 mL by centrifugal filtration using an Amicon Ultra-15 (10 kDa) spin filter. EV populations were size-separated by fast protein liquid chromatography (FPLC). FPLC fractions corresponding to the size range of exosomes (50–150 nm) were collected and suspended into approximately 1 mL of  $0.5\times$  PBS. The concentration and size distribution of collected EVs were measured using a qNano gold instrument by IZON (Christchurch, New Zealand).

Size distribution and concentration data were plotted in Fig. S1.† Harvested EVs were aliquoted and stored at  $-80\text{ }^{\circ}\text{C}$ .

**2.1.3 Positive controls were created by spiking EVs and fluorescent NPs into blood plasma.** One whole blood sample from a healthy donor was obtained from the OHSU Knight Cancer Institute Cancer Early Detection Advanced Research (CEDAR) center biorepository (IRB approval #00018048) where written informed consent was obtained. All experimental protocols were carried out in accordance with federal and state regulations, and relevant policies as outlined by OHSU and the OHSU IRB. The OHSU IRB determined that the activity of this study (IRB #00018572) was not research involving human subjects. Blood plasma from the single healthy human patient was acquired through centrifugation of fresh blood stored in EDTA (1500g for 15 minutes at  $4\text{ }^{\circ}\text{C}$ ). The first set of experiments was designed to

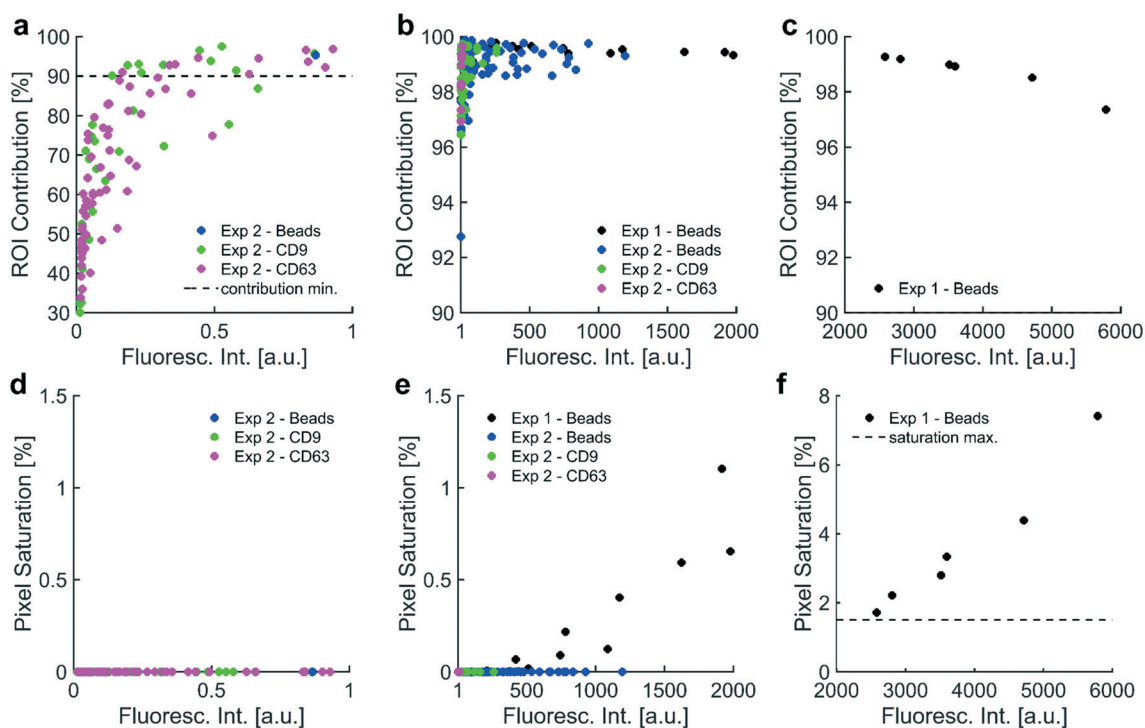


**Fig. 2** Data quality metrics informed a usable dynamic range in fluorescence intensity: two data quality metrics, contribution from the ROI and pixel saturation, were plotted against three sets of fluorescence intensity values. Contribution from the ROI indicated the percentage of the intensity value that originated from pixels in the ROI, which was the collection region under high-field DEP. Fluorescence intensity values needed a minimum contribution from the ROI of 90% to ensure most of the value was attributed to signal from collected particles. Pixel saturation indicated the percentage of saturated pixels used to calculate each fluorescence intensity value. A maximum allowable pixel saturation of 1.5% ensured that saturation did not adversely affect quantitation. a) Fluorescence intensities in the set [0, 1 a.u.] showed a positive correlation ( $r = +0.717$ ) with increasing contribution from ROI. Most intensities were below the 90% cutoff for contribution from the ROI. b) All fluorescence intensities in the set [1 a.u., 2000 a.u.] exhibited contributions from the ROI greater than 90%. There was a weak correlation ( $r = +0.261$ ) between increasing fluorescence intensity and contribution from the ROI over this set of intensities. c) In the range [2000 a.u., 6000 a.u.], there existed a strong negative correlation ( $r = -0.960$ ) between fluorescence intensities and contribution from the ROI. Increasingly high fluorescence at the ROI could have generated photonic noise, which likely bled into the BG, reduced the contribution from the ROI, and caused the negative correlation between fluorescence intensity and ROI contribution over this set of intensities. Importantly, all intensities between [2000 a.u., 6000 a.u.] exhibited contributions from the ROI above 90%. d) Fluorescence intensities in the set [0, 1 a.u.] did not correlate with pixel saturation as no saturation was detected. e) All intensities in the set [1 a.u., 2000 a.u.] exhibited minimal pixel saturation (lower than 1.5%), meeting the second quality criterion. Fluorescence intensities correlated ( $r = +0.746$ ) with pixel saturation over this set; however, pixel saturation was sufficiently low (less than 1.5%) for all values. f) There existed a strong positive correlation ( $r = +0.976$ ) between fluorescence intensities in this set [2000 a.u., 6000 a.u.] and pixel saturation. All intensities in this set exhibited pixel saturation rates above 1.5%, indicating that saturation could adversely affect quantitation. Contribution from the ROI and pixel saturation rates suggested that the usable dynamic range of intensities was [1 a.u., 2000 a.u.].



determine the dynamic range of the system. These experiments involved spiking varying concentrations of fluorescent polystyrene NPs into the plasma and then collecting the particles *via* DEP. Images were acquired in multiple fluorescence channels and quantified using the technique described in this paper. Fluorescence intensities from the first set of experiments were plotted in Fig. 2 (“Exp 1”) and Fig. 3a and b. Plotted fluorescence intensities were calculated from fluorescence images obtained over three experiments.

The second experiment was designed to investigate the influence of the internal standard (*i.e.* a fixed concentration of fluorescent polystyrene NPs) on varying concentrations of immunolabeled EVs each run as technical triplicates (“Exp 2” in Fig. 2, 3c–f, and 5). HeLa-derived EVs were incubated with mouse monoclonal anti-CD9-Alexa Fluor 488 antibody for one hour at room temperature (1:50 dilution from stock). Immunolabeled EVs were diluted serially into healthy human plasma ( $2 \times 10^{10}$ ,  $4 \times 10^{10}$ ,  $8 \times 10^{10}$  EVs mL<sup>-1</sup>). Fluorescent polystyrene NPs were added to a final concentration of approximately  $5 \times 10^9$  particles per mL in each plasma dilution of EVs. Technical triplicates of each dilution were loaded into three physically isolated microfluidic chambers on DEP chips. Fluorescent NPs and EVs were simultaneously collected *via* DEP with subsequent immunostaining, fluorescence image acquisition, and image quantification. Fluorescence intensities from the second experiment were also used to determine the dynamic range of the system.

#### 2.1.4 NP collection from plasma *via* dielectrophoresis.

Microfluidic chambers on DEP chips were first hydrated with 0.5× PBS to prepare the hydrogel layer prior to loading blood plasma samples. Forty microliters of plasma were drawn into the chamber prior to applying electrical signal to generate DEP forces at the electrodes in the bottom plane of the chamber (15 kHz; 12 V<sub>pp</sub>; 15 min). EVs and fluorescent polystyrene NPs were collected simultaneously in experiments involving the internal standard (“Exp 2”); otherwise, only fluorescent polystyrene NPs were collected (“Exp 1”). Samples were washed with 0.5× PBS to remove the bulk plasma. The collected material was blocked using 2% by-weight Difco skim milk powder in 0.5× PBS for 30 minutes to reduce nonspecific antibody binding. Samples were washed with 0.5× PBS to remove blocking buffer. For experiments involving the internal standard, the collected EVs and NPs were incubated for one hour at room temperature with 40 microliters of a 1:50 dilution from stock of mouse monoclonal anti-CD63-Alexa Fluor 647 primary antibody added into blocking buffer (“Exp 2”). Samples were washed with 0.5× PBS. Samples spiked with only fluorescent polystyrene NPs were not incubated with antibodies (“Exp 1”). For SEM imaging, the 0.5× PBS in the microfluidic chamber of the chip was exchanged for 1× TE buffer prior to freezing the DEP chip using dry ice and an aluminum block stored at -80 °C.

**2.1.5 Endogenous NPs were isolated from patient plasma and immunofluorescently labeled.** The third experiment was designed to evaluate whether automated artifact removal could reproduce fluorescence intensities obtained *via* a

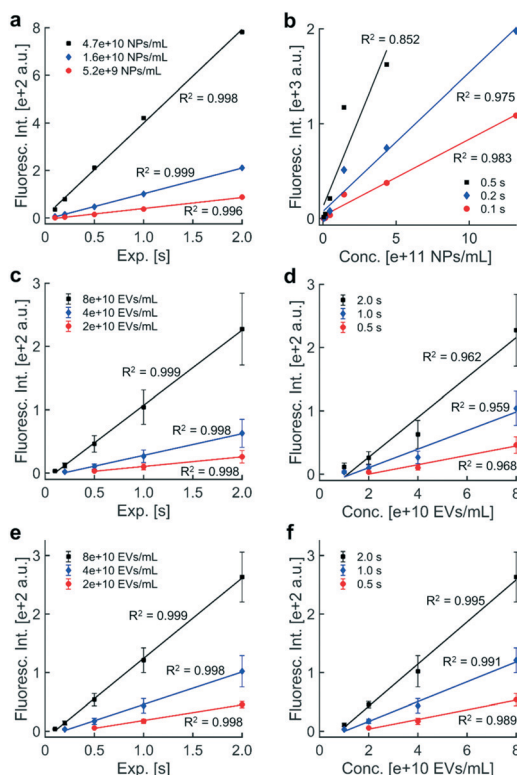


**Fig. 3** Fluorescence intensity increased linearly with exposure time and with particle concentration: trends in exposure time and particle concentration were assessed for fluorescence intensities in panels a through d and for intensities adjusted to the internal standard in panels e through f. a) Fluorescence intensities of fluorescent polystyrene NPs collected *via* DEP from healthy human plasma were plotted against exposure time at three contours in particle concentration ( $0.52$ ,  $1.6$ ,  $4.7 \times 10^{10}$  beads per mL). Best-fit lines through intensities within the dynamic range indicated that the data followed linear trends. b) Fluorescence intensities from images of fluorescent polystyrene NPs were plotted against particle concentration for three contours in exposure time (0.1, 0.2, 0.5 s). Best-fit lines were plotted through fluorescence intensities within the dynamic range, indicating that fluorescence intensity increases linearly with the concentration of fluorescence particles. c) Fluorescence intensities of immunofluorescently labeled EVs collected *via* DEP from healthy human plasma were plotted against exposure time at three contours in particle concentration ( $2$ ,  $4$ ,  $8 \times 10^{10}$  EVs mL<sup>-1</sup>). Data points represented the mean fluorescence intensity across three technical replicates. Replicates were analyzed in separate microfluidic chambers on DEP chips. Error bars represented one standard deviation above and below the mean fluorescence intensity. Linear fits were calculated using mean intensities within the dynamic range, confirming that fluorescence intensity increases linearly with exposure time. d) Fluorescence intensities of immunofluorescently labeled EVs plotted against EV concentration as contours in exposure time (0.5, 1.0, 2.0 s). The physical presence of the internal standard did not affect the linear relationship between fluorescence intensity and EV concentration. e) Chip-to-chip differences in collection efficiency caused variability in fluorescence intensity across technical triplicates in panel c. An internal standard was used to quantify the collection efficiency of each DEP chip. A known concentration of fluorescent polystyrene NPs were spiked into each plasma sample containing EVs. EVs and NPs were simultaneously recovered by DEP. Adjusting the EV signal to the internal standard did not change the linear relationship between fluorescence intensity and EV concentration. f) Use of the internal standard improved the coefficient of determination for each best-fit line in panel d and reduced variability in fluorescence intensity caused by differences in collection efficiency across DEP chips.



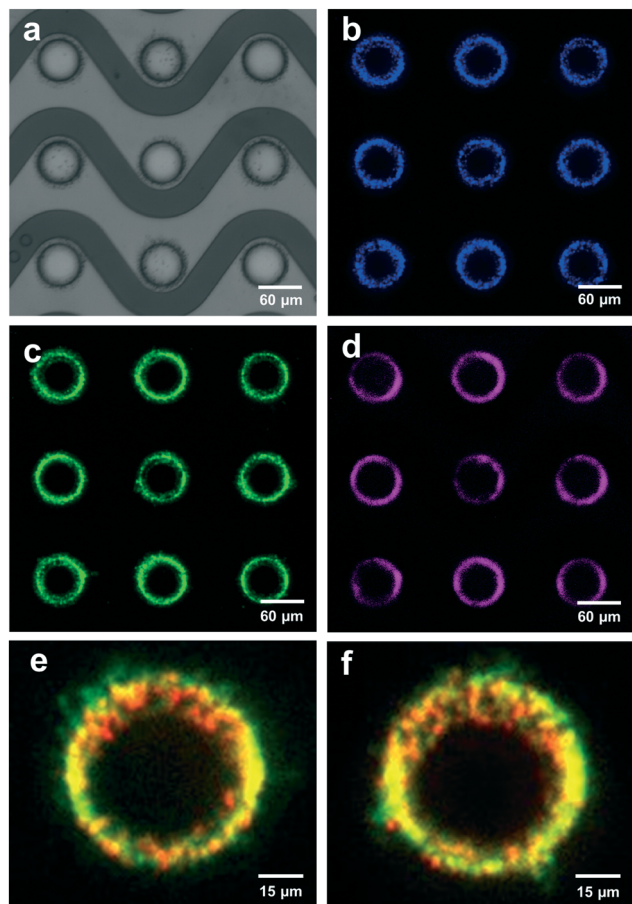


**Fig. 4** Fluorescently labeled NPs were collected at high-field DEP regions: four images of the same field-of-view were acquired through different optical filters to demonstrate the simultaneous recovery of multiple particle types from healthy human plasma in the high-field regions around the electrode edge *via* DEP. a) A bright field image showed nine planar, circular electrodes on the DEP chip. b) A DAPI channel image indicated the collection of spiked fluorescent polystyrene NPs (100 nm diameter) collected in high-field regions from healthy human plasma *via* DEP (contrast-enhanced). c) An EGFP channel image showed the presence of HeLa-derived EVs, which were immunolabeled with anti-CD9-Alexa Fluor 488 and spiked into the same healthy human plasma prior to collection *via* DEP (contrast-enhanced). d) A Cy5 channel image of the same HeLa-derived EVs, which were immunolabeled with anti-CD63-Alexa Fluor 647 after collection (contrast-enhanced). e and f) Representative composite images of two electrodes showed the collected polystyrene NPs in red and the collected EVs in green. There was a strong positive spatial correlation between the two, shown in yellow, with a Pearson's  $R$  value of  $0.75 \pm 0.03$  (mean  $\pm$  standard deviation,  $n = 10$ ). This correlation indicated that the spatial collection of the 100 nm polystyrene NPs accurately reflected the spatial collection of the EVs.

controlled process of manual artifact removal (Fig. 6). Thirty-six clinical plasma samples were obtained from the OHSU interventional endoscopy unit under the Oregon Pancreas Tissue Registry (IRB approval #00003609) with use under OHSU IRB approval #00018572. Informed consent was obtained from all subjects. All experimental protocols were carried out in accordance with relevant guidelines and regulations outlined by the OHSU Institutional Review Board.

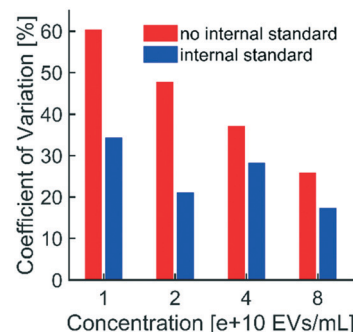


**Fig. 5** Use of the internal standard reduced non-physiological variability in fluorescence intensity: EVs and fluorescent polystyrene NPs (internal standard) were spiked into healthy human plasma, isolated simultaneously *via* DEP in technical triplicates, and imaged at an exposure of 1.0 s. Unadjusted fluorescence intensities of technical triplicates were averaged and standard deviations were calculated at each of four EV concentrations. CVs were calculated at each concentration of EVs (plotted in red). Fluorescence intensities from EVs were also adjusted to corresponding intensities from the internal standard. CVs for adjusted intensities were calculated (plotted in blue). CVs of adjusted intensities were lower than the CVs of unadjusted intensities at all concentrations of EVs, indicating that the internal standard effectively reduced non-physiological (*i.e.* technical replicate) variability in fluorescence intensity. Reductions in variability were most substantial at lower concentrations of EVs, suggesting that use of the internal standard could be critical at the low biomarker concentrations typical of early-stage disease.

Proprietary hydrogel layers in the microfluidic chambers of the DEP chips were treated with  $0.5\times$  PBS. Thirty microliters of sample were drawn into each microfluidic chamber. HeLa-derived EVs and other endogenous NPs were collected *via* DEP (14 kHz; 10  $V_{pp}$ ; 15 min) from all samples. Collected material was stained for one target after blocking with 2% by-weight milk powder in  $0.5\times$  PBS for one hour. Collected material was labeled for the second target using a primary–secondary antibody stain. Material was incubated with the primary antibody solution (1:200 dilution from stock) into blocking buffer for one hour at room temperature prior to washing with  $0.5\times$  PBS. Material was incubated with a fluorescently-labeled secondary antibody solution (1:500 dilution from stock into blocking buffer) for one hour at room temperature prior to washing with  $0.5\times$  PBS.

**2.1.6 Scanning electron microscopy of DEP chips used to collect EVs and NPs.** DEP chips for scanning electron microscopy were flash-frozen by placing ground dry ice on top of the plastic cover of the chip before placing the chip on top of an aluminum block stored at  $-80^\circ\text{C}$ . After the plastic covers were removed, the chip was lyophilized and the microelectrode arrays on the surfaces of DEP chips were coated with a conductive layer. Micrographs of DEP chips were acquired with a NanoLab Helios 660 from FEI (Lausanne, Switzerland) at an operating voltage of 2.0 kV.

**2.1.7 Image acquisition.** Bright field and fluorescence images were acquired at a field-of-view centered in the middle of each microfluidic chamber using DAPI, EGFP, and Cy5 fluorescence filters at five different exposures (0.1, 0.2,



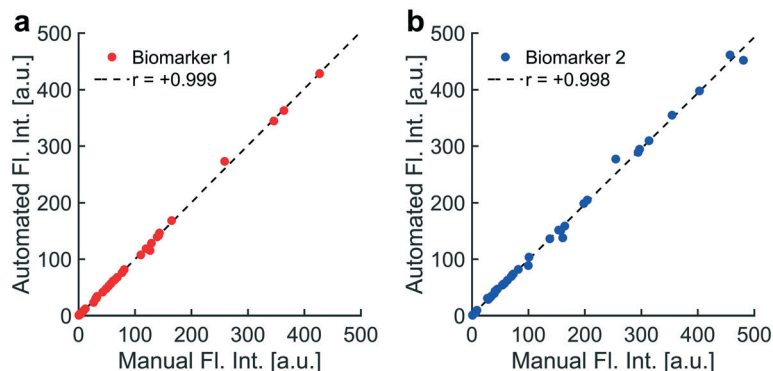


**Fig. 6** Automated artifact removal was faster and as accurate as manual artifact removal: implementation of automated artifact removal was compared to a standard protocol for manually removing artifacts by assessing correlations in fluorescence intensities resulting from both methods. Plasma samples from thirty-six patients were analyzed for the presence of two biomarkers. Each data point represented a fluorescence image of one immunolabeled biomarker collected from the plasma of a single patient. a) One biomarker was fluorescently labeled on endogenous NPs collected from blood plasma of thirty-six patients. Fluorescence images were acquired and analyzed using two methods: a standard procedure for manually removing bright field and fluorescence artifacts (“Manual Fl. Int.”) and a programmatic implementation of that standard procedure for artifact removal (“Automated Fl. Int.”). A strong positive correlation between manual and automated intensities suggested that automatic artifact removal was as accurate as manual removal (biomarker 1:  $r = +0.999$ ). b) A second biomarker was fluorescently labeled on endogenous NPs. Manual and automated intensities for the second biomarker also correlated strongly (biomarker 2:  $r = +0.998$ ). Automatic artifact removal saved substantial amounts of time for users and minimized user biases, reducing analytical error across experiments.

0.5, 1.0, and 2.0 s, respectively). The X-Cite 120LED Boost light source from Excelitas Technologies (Waltham, MA) was used at 100% intensity during fluorescence imaging and at 5–7% intensity for bright field imaging. Images were acquired with 14 bit resolution using an Axiocam 506 camera affixed to an Axio Imager A2 fluorescence microscope from ZEISS (Oberkochen, Germany). All images were acquired using a 5 $\times$  magnification objective lens (Objective EC “Plan-Neofluar” 5 $\times$ /0.16 Ph1 M27; #420331-9911-000) from ZEISS (Oberkochen, Germany). Catalog set 39000 (AT375/28 $\times$  excitation, AT415DC beam splitter, AT460/50 m emission), catalog set 39002 (AT480/30 $\times$  excitation, AT505DC beam splitter, AT535/40 m emission), and catalog set 39007 (AT620/50 $\times$ , AT655DC beam splitter, AT690/50 M emission) filters from Chroma Technology (Bellows Falls, VT) were used for image acquisition in the DAPI, EGFP, and Cy5 fluorescence channels, respectively. Gamma and analog gain were set to unity for image acquisition. Images were acquired with 6.07 megapixel resolution (2752  $\times$  2208 pixels). All fluorescence images corresponding to data shown in this paper were acquired from samples in 0.5 $\times$  PBS prior to using 1 $\times$  TE buffer for chip storage at  $-80$   $^{\circ}$ C. Fluorescence images were exported as uncompressed, unedited, greyscale TIFs (16 bit depth) using ZEN 2.3 Blue software from ZEISS. Fluorescence images were quantified with custom image-processing software written in MATLAB<sup>®</sup><sup>43</sup> on a Microsoft Windows 10 operating system (Enterprise version 10.0; build 15063). Fluorescence quantification for this custom software required pixel values represented in 16 bit depth.

**2.1.8 Theoretical simulation of DEP high-field regions in a planar microelectrode array.** The gradient distribution of the electric field squared was simulated in COMSOL (Los Angeles, CA) using a model of 60  $\mu$ m diameter electrodes on a 150  $\mu$ m spacing. The simulated fluid was modeled with a

conductivity of 1.4 S  $m^{-1}$  and a relative permittivity of 80. The fluid height extended 200  $\mu$ m from the electrode floor. Boundary conditions were set to assume an infinite array of electrodes. Electrode polarity alternated in a checkerboard pattern of 0 V and 10  $V_{rms}$ , respectively.

## 2.2 Design of algorithm for optical quantification

**2.2.1 Algorithm input consisted of pairs of fluorescence and bright field images.** This section references Fig. 7a and S2i–v.<sup>†</sup> CZI files were exported from Zen 2.3 lite (blue edition) with parameters described in ESI<sup>†</sup> section S1.1 (Fig. S2i). The executable (.exe) version of the software was opened (Fig. S2ii<sup>†</sup>). The software prompted the user to select the folder (ANALYZE ME) containing image pairs for quantification. The user was not prompted for additional information after this step (Fig. S2iii<sup>†</sup>). Experiment folders, image folders, and individual images were automatically indexed. Bright field images were paired with each of between one and four fluorescence channel images (Fig. S2iv<sup>†</sup>). The first pair of bright field and fluorescence images were inputted into data structures as two-dimensional sets of 16 bit pixel intensity values (Fig. S2v<sup>†</sup>).

**2.2.2 Electrode locations were identified using bright field images.** This section references Fig. 7b and S2vi and vii.<sup>†</sup> Two Hough transforms were conducted using the `imfindcircles` function<sup>44</sup> to identify circular objects in the bright field image that resembled electrodes (60  $\mu$ m diameter) under a 5 $\times$  objective lens. Each transform yielded a set of potential electrode locations (yellow circles in Fig. 7b; “Set 1” and “Set 2” in Fig. S2vi<sup>†</sup>) from a single bright field image. An area encompassing the electrode and surrounding BG was defined at the center of each electrode (yellow squares in Fig. 7b). All pixel values were extracted from these square areas (Fig. S2vii<sup>†</sup>).



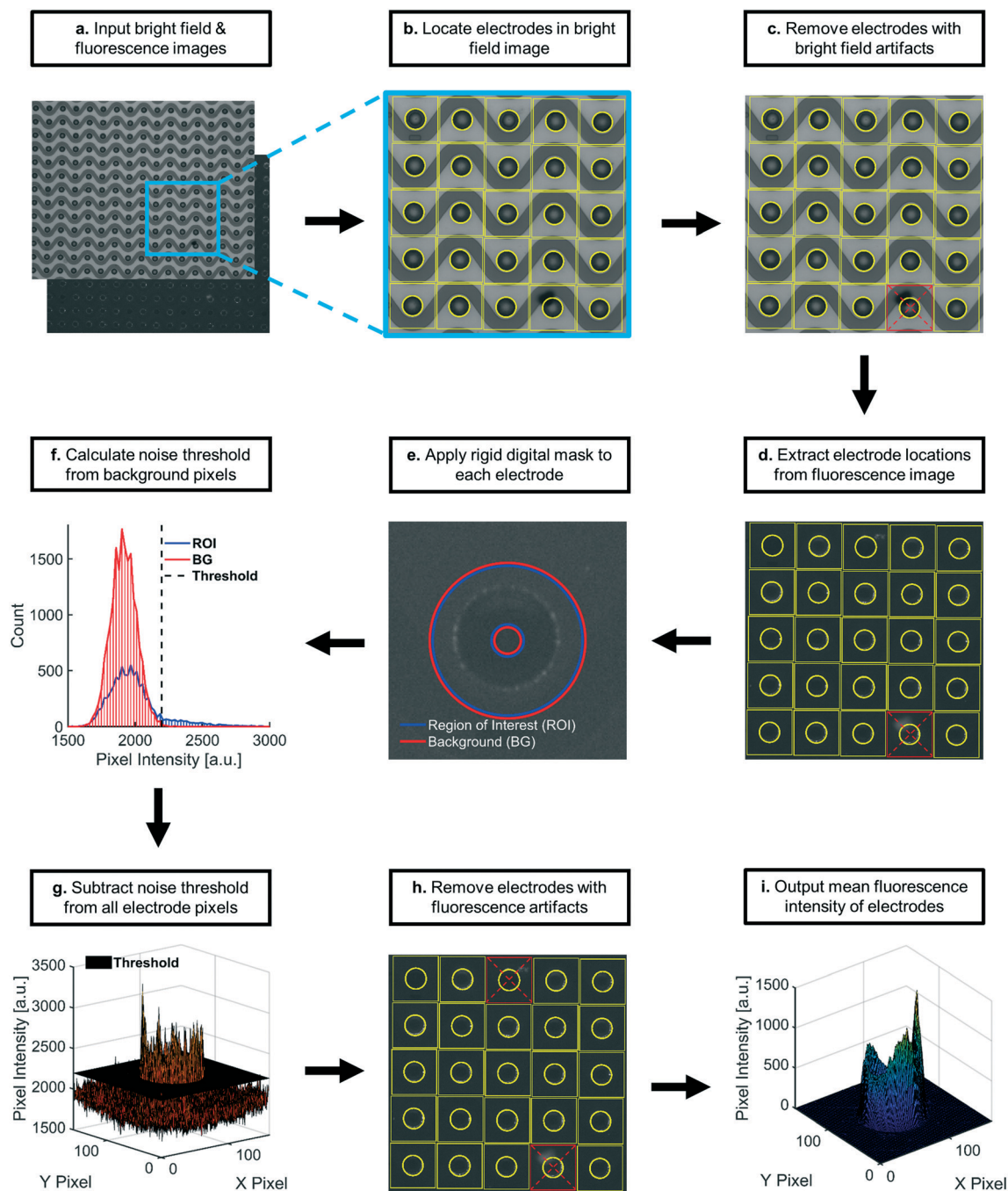


**Fig. 7** Process flow diagram for automated fluorescence quantification: a) pairs of corresponding bright field and fluorescence images were inputted and indexed. b) Electrode locations were identified using the bright field image. c) Electrode locations were assessed for usability. Usable electrodes were those centered within  $160 \times 160$  square pixel areas, none of which overlapped. Electrodes with optical artifacts were removed from analysis. d) Usable electrode locations were transferred to the paired fluorescence image. Square regions centered at each electrode were extracted. e) A rigid digital mask was applied to each square region, categorizing pixels as either ROI (regions of high-field DEP) or BG (regions of low-field DEP). f) Intensity distributions of BG pixels were used to calculate noise thresholds specific to each square region. g) The noise threshold value was subtracted from all pixels in respective square regions. The average fluorescence intensity was calculated for each noise-subtracted square region. h) Square areas containing apparent fluorescence artifacts were removed from downstream analysis. i) The average intensity at each remaining electrode was then used to calculate the sample mean fluorescence intensity, which constituted the data points plotted in all figures for this paper. All essential calculations and relevant metadata were saved in reports that were automatically generated after each image pair was analyzed. The described processes repeated for remaining image pairs.

**2.2.3 Unusable electrodes with bright field artifacts were removed from analysis.** This section refers to Fig. 7c and

S2viii–xii.† Electrodes at the perimeter of the field-of-view that lacked sufficient pixel counts were removed from the two sets



of potential electrode locations (Fig. S2viii and ix†). The DEP chip electrode array was on a regular pattern, allowing us to maximize the extraction area (yellow squares in Fig. 7) while avoiding overlap. Overlap indicated misidentification of optical artifacts as electrodes. All overlapping areas of identification were removed from the set of potential electrodes that contributed to downstream quantitative calculations (Fig. S2x and xi†). After all bright-field artifacts and affected electrodes had been removed, the larger of the two sets of potential electrodes from the two Hough transforms was selected for additional processing (Fig. S2xii†).

**2.2.4 A rigid digital mask differentiated the ROI from BG at each electrode.** This section refers to Fig. 7d and e and S2xiii, xv and xvi.† The selected set of electrode locations was transferred to the paired fluorescence image (Fig. 7d and S2xiii†). All pixel values at each electrode location were extracted (yellow squares in Fig. 7d and S2xv†). A rigid digital mask with fixed geometry was applied to each extracted location, categorizing pixels as either ROI or BG (Fig. S2xvi†). Theoretical simulations and empirical observation (Fig. 1) informed the geometry of the mask based on ring-shaped patterns of particle collection at areas of high-field DEP. The ROI entirely encompassed the circumference of the planar electrode, or high-field region, where particles of interest collect under pDEP. The BG encompassed low-field regions surrounding the electrode and at the center of the electrode, away from where particles moved under pDEP. Fluorescence intensity of collected material was determined by comparing pixel intensities in the ROI (high-field region) to pixel intensities in the BG (low-field region).

**2.2.5 Local noise thresholds were calculated from BG pixels and subtracted from all pixels at each electrode.** This section references Fig. 7f and g and S2xvii–xxi.† Pixels from the BG region of each electrode location were used to calculate noise threshold values specific to each electrode. BG pixels exhibited lognormal intensity distributions and were logarithmically transformed (Fig. 7f and S2xvii†). Transformed mean and standard deviation values were used to estimate mean and standard deviation values (Fig. S2xviii†). Noise thresholds at each electrode location equaled the estimate of the mean plus three times the estimate of the standard deviation (Fig. S2xix†). Local noise thresholds were subtracted from all pixels in each respective electrode location (Fig. 7g and S2xx†). The average pixel intensity was calculated using all pixels in each noise-subtracted electrode location (Fig. S2xxi†).

**2.2.6 Unusable electrodes with fluorescence artifacts were removed from analysis.** This section refers to Fig. 7h and S2xiv, xxii and xxiii.† A global intensity threshold was calculated as six standard deviations above the average pixel intensity of the entire inputted fluorescence image (Fig. S2xiv†). If at least 99.9% of BG pixels around a single electrode had intensities lower than the global intensity threshold, the electrode remained in the set (Fig. S2xxii and xxiii†). Otherwise, the electrode likely exhibited at least

one fluorescence artifact and was removed from the set (Fig. 7h).

**2.2.7 Fluorescence intensity was calculated from usable electrodes.** This section references Fig. 7i and S2xxiv–xxviii.† The average pixel intensities of each noise-subtracted electrode remaining in the usable set after artifact removal were then averaged to calculate the overall mean fluorescence intensity, referred to throughout the paper as “fluorescence intensity” (Fig. S2xxiv†). The population mean of the average pixel intensity of all noise-subtracted electrodes in the microfluidic chamber of the DEP chip was estimated within 95% confidence bounds (Fig. S2xxv†). Warnings regarding data quality were displayed in the command window for the user when relevant (Fig. S2xxvi†). These warnings included: a low contribution to fluorescence intensity from the ROI, a fluorescence intensity below the lower detection limit of 1 a. u., fewer than 100 electrodes used to calculate fluorescence intensity, and a high rate of pixel saturation. Calculations, image data, quality control metrics, warnings, and metadata were compiled into a report, which was automatically generated, indexed, and saved to the respective image folder (Fig. S2xxvii†). All information extracted and calculated from the first pair of input images was cleared from memory. The next indexed pair of images were inputted automatically. The described process repeated until all images were analyzed. The custom MATLAB® code can be found in ESI.† Posts on the MATLAB Answers online forum<sup>45</sup> were accessed during the development of the algorithm.

### 2.3 Statistical analyses

“Fluorescence intensity” refers to the sample mean of the average fluorescent pixel intensity from noise-subtracted areas at each usable electrode in a field-of-view. The “sample” refers to as many as 208 usable electrodes in the field-of-view of the input image. The quantified sample was a subset of the total population of electrodes in the microfluidic chamber of the chip. The population mean was estimated from the sample of usable electrodes to within 95% confidence (included in automated reports; confidence intervals not plotted). To obtain technical triplicates, three aliquots from one biological sample were obtained. Each aliquot was introduced to a single microfluidic chamber prior to collection of particles *via* DEP, immunofluorescence labeling, washing, and imaging. Variability in fluorescence intensity across technical triplicates represented differences between individual populations of electrodes. Error bars in plotted data represented one standard deviation above and below the average fluorescence intensity of technical triplicates (*i.e.* three quantitative values from three input images, each representing one of three technical replicates).

Pearson correlations between variables on vertical and horizontal axes were calculated for subplots in Fig. 2 and 6. Linear fits in Fig. 3 were calculated using plotted fluorescence intensities, all of which were within the usable dynamic range (1–2000 a.u.). Fluorescence intensities in



Fig. 3c and d were adjusted for collection efficiency using the internal standard and plotted in Fig. 3e and f. To adjust for collection efficiency, the fluorescence intensity of the internal standard for one sample (“reference”) was arbitrarily selected. Correction factors were calculated by dividing the reference intensity by the measured intensities of the internal standard in each sample (e.g. such that the correction factor for the reference sample was one). The fluorescence intensity of the target biomarker in each sample was then multiplied by the correction factor. Unique sets of correction factors were calculated for each exposure time. Coefficients of variation (CVs) were calculated for technical triplicates in unadjusted and adjusted fluorescence intensities (Fig. 5).

#### 2.4 Automation of software for optical quantification

Previous script versions relied on user input to identify artifacts for removal, which introduced several sources of analytical error. Optical artifacts included debris or bubbles on top of or inside the microfluidic chamber that had abnormally high levels of fluorescence through one or more optical filters. Multiple users could have different interpretations as to whether a given set of pixels qualified as an artifact. These discrepancies were present even amongst users following the same protocol for identifying artifacts. Another source of error could arise within a single user whose interpretation of the protocol for artifact identification changed subconsciously over time. These user biases added a potential source of error in measurements of fluorescence intensity. Manual artifact removal also required substantial amounts of time from users, reducing throughput.

To address these issues, we developed an algorithm that automated the removal of optical artifacts from images. To evaluate the performance of the automated system, we acquired a set of fluorescence images of two labeled biomarkers isolated from the plasma of thirty-six patients (72 images total). This set of images was analyzed using both the manual and automated approaches, the results of which were compared in Fig. 6. The manual approach outlined a protocol for identifying and removing optical artifacts while minimizing user bias. The protocol required that a single user needed to perform the analysis in less than three days in order to minimize drift in the user's interpretation of the protocol. The automated approach was designed to mimic the user protocol by programmatically encoding artifact removal into the software.

#### 2.5 Metrics of data quality

In order to develop a robust, automated method for quantification of collected EV biomarkers, it was necessary to establish metrics for data quality within the optical analysis software. Analysis of these data quality metrics enabled us to define a dynamic range of fluorescence intensity values that

exhibited consistent, quantitative trends with both exposure time and particle concentration. The first quality metric was the percentage of the fluorescence intensity that originated from the ROI. This metric was used to ensure that the fluorescence intensity in the ROI was substantially higher than the surrounding BG. We overlaid all the identified electrode areas (yellow boxes in Fig. 7) and averaged respective pixels to generate a representative image of the average electrode. We categorized ROI and BG pixels in the averaged electrode image with the same digital mask we used to calculate noise levels at individual electrodes (Fig. 7e and S2xvi†). We integrated pixel intensities within the ROI as well as intensities within the BG, noting that the sum of the two integrals equaled the fluorescence intensity value. Both fluorescent polystyrene NPs and immunolabeled EVs were collected using DEP, quantified, and presented in Fig. 2. Fluorescence intensities above 1 a.u. consistently exhibited contributions from the ROI of at least 90% (Fig. 2a–c). Therefore, we set the cutoff for the contribution from the ROI to the overall fluorescence intensity to be greater than 90%.

The second metric for data quality was the percentage of saturated pixels contributing to the fluorescence intensity. Due to inherent limitations of the camera, a saturated pixel indicated that the upper limit of incident photons had been recorded. Photons subsequently incident upon the photodetector were not measured, leading to an underestimation of fluorescence. For this reason, reliable data required negligible numbers of saturated pixels. From the data shown in Fig. 2f, fluorescence intensities above 2000 a.u. showed a strong positive correlation with pixel saturation. Intensities in this set of values exhibited saturation rates above 1.5%. Therefore, the second condition for high-quality data was that the pixel saturation rate must be less than 1.5%.

## 3. Results & discussion

### 3.1 Automation of software for optical quantification

**3.1.1 Automatic artifact removal is preferred to manual artifact removal.** We evaluated the impact of automated artifact removal on the accuracy of quantifying fluorescence images. Two critical sections of the described algorithm were devoted to the identification and removal of bright field and fluorescence artifacts from analysis of fluorescence intensity around the circumference of the electrodes (Fig. 7c and h and S2viii–xi and xxii†). Fluorescence intensities from automated artifact removal were plotted against the intensities from manual artifact removal for two fluorescently labeled biomarkers (Fig. 6). Bivariate correlations were performed separately for each biomarker. Automated and manual methods yielded fluorescence intensities that correlated strongly for biomarker 1 ( $r = +0.999$ ) and biomarker 2 ( $r = +0.998$ ), confirming that the automated system worked as well as manual artifact removal. We used



automated artifact removal for the analysis of the data presented in this paper.

### 3.2 Characterization of software for optical quantification

**3.2.1 Metric of data quality for the lower limit of the dynamic range.** Data points plotted in Fig. 2 were referred to as “fluorescence intensity,” where each value quantitates the average fluorescence signal from up to 208 locally noise-subtracted electrodes in a single field-of-view. The data quality metric for the lower limit of detection was the percentage of the fluorescence intensity originating from the ROI. Both fluorescent polystyrene NPs and immunolabeled EVs were collected using DEP, quantified, and presented in Fig. 2. Fluorescence intensities above 1 a.u. consistently exhibited contributions from the ROI of at least 90% (Fig. 2a–c). We noticed empirically during algorithm optimization that fluorescence intensities less than 1 a.u. yielded low signal at the ROI that was usually undiscernible from noise in the BG. Therefore, we set the cutoff for acceptable contributions from the ROI to be greater than 90%.

Fluorescence from collected particles in the ROI showed a discernible ring-shaped pattern where simulations suggested the accumulation of biomarkers that were responsive to pDEP. We wanted to elucidate the lower limit of fluorescence intensity values that correlated with high contributions from the ROI (*i.e.* above 90%) to yield ring-shaped fluorescence patterns. When there was no difference in the distribution of pixel intensities in the ROI (high-field DEP) and the distribution of pixel intensities in the BG (low-field DEP), there was no discernible pattern of fluorescence after noise-subtraction. Assuming a Gaussian noise distribution of pixel intensities spanning the ROI and BG, the contribution from the ROI to the fluorescence intensity should have been approximately 31% because the BG contained approximately 2.2 times as many pixels as the ROI ( $1/(2.2 + 1) = 0.31$ ). ROI contributions of 31% therefore indicated pure noise, and fluorescence intensities with contributions from the ROI greater than 31% contained some signal. We empirically decided that contributions from the ROI needed to be at least 90% for patterns of fluorescence to be discernible. The contribution from the ROI could not equal 100% because the process for thresholding noise eliminated approximately 99.7% of pixels in the BG (assuming a normal distribution of pixel intensities). Therefore, approximately 0.3% of pixels in the BG would always contribute to fluorescence intensity values, meaning that there would always be a nonzero BG contribution and a non-unity contribution from the ROI. Therefore, fluorescence intensity values indicative of NP collection should have had contributions from the ROI in the set of percentages [90, 100]. Furthermore, fluorescence intensity values would be greater than zero because there would always be a nonzero level of BG noise, regardless of exposure time during image acquisition and the amount of fluorescent particles isolated *via* DEP.

Pearson coefficients were calculated to assess correlations between contribution from the ROI and fluorescence intensity over three sets of intensity values. Fluorescence intensity values in the set [0, 1 a.u.] correlated strongly with contribution from the ROI ( $r = +0.717$ ; Fig. 2a). Contribution from the ROI tended toward approximately 30% as fluorescence intensities approached zero. Both observations agreed with expectations: contribution from the ROI increased as fluorescence intensity increased, ranging from pure noise (approximately 30%) for intensities approaching zero to fluorescence patterns (at or above 90%) for intensities approaching 1 a.u. Fluorescence intensities in the set [1 a.u., 2000 a.u.] correlated weakly with contribution from the ROI ( $r = +0.261$ ; Fig. 2b). Fluorescence intensities in this set were also exclusively above the cutoff for detectable fluorescence (contribution from ROI greater than or equal to 90%), meaning that all intensities in the set [1 a.u., 2000 a.u.] exhibited patterns of ring-shaped fluorescence. Fluorescence intensities in the set [2000 a.u., 6000 a.u.] demonstrated a strong negative correlation with contribution from the ROI; however, all intensities in the set [2000 a.u., 6000 a.u.] exhibited discernible patterns of ring-shaped fluorescence through contributions from the ROI above 90% ( $r = -0.960$ ; Fig. 2c). The unanticipated negative correlation was likely caused by increasing amounts of photon noise leaking into the BG region from increasingly strong signal at the ROI (Fig. 7e).

**3.2.2 Metric of data quality for the upper limit of the dynamic range.** The percentage of saturated pixels contributing to the fluorescence intensity was the data quality metric for the upper limit of the dynamic range. From the data shown in Fig. 2f, fluorescence intensities above 2000 a.u. showed a strong positive correlation with pixel saturation. We also observed that fluorescence intensities above 2000 a.u. were usually associated with regions of adjacent pixels that formed saturated intensity plateaus. Most intensities above 2000 a.u. corresponded to pixel saturation rates above 1.5%. Therefore, the second condition for high-quality data was that the pixels saturation rate must be less than 1.5%.

Pearson coefficients were calculated to ascertain correlations between the amount of pixel saturation and fluorescence intensity over three sets of intensity values. We determined that the population of saturated pixels needed to be at or below 1.5% for the fluorescence intensity value to be quantitative. All images were acquired with a 14-bit camera and exported as 16-bit TIFs. The multiplicative conversion from 14-bit format to 16-bit did not change the resolution of the image as the relative spacing between adjacent intensity values remained the same.

Fluorescence intensities in the set [0, 1 a.u.] did not correlate with pixel saturation because no saturation was detected (Fig. 2d). Fluorescence intensity over the set [1 a.u., 2000 a.u.] positively correlated with pixel saturation, as expected ( $r = +0.746$ ; Fig. 2e). Fluorescence intensities in this set were exclusively below 1.5% pixel saturation. Fluorescence



intensities in the set [2000 a.u., 6000 a.u.] demonstrated a strong positive correlation with rates of pixel saturation ( $r = +0.976$ ; Fig. 2f). Pixel saturation rates for fluorescence intensities in this set exceeded 1.5%, confirming that substantial pixel saturation was prevalent in fluorescence intensities above 2000 a.u.

**3.2.3 Usable dynamic range.** Based on these observations, we concluded that the usable dynamic range over which fluorescence intensities exhibited consistent, quantitative trends with both exposure time and particle concentration would exist between 1 and 2000 a.u. We tested correlations with fluorescence intensities and data quality metrics over three sets of intensity values: [0, 1 a.u.] in Fig. 2a and d; [1 a.u., 2000 a.u.] in Fig. 2b and e; and [2000 a.u., 6000 a.u.] in Fig. 2c and f. All fluorescence intensities in the set [1 a.u., 2000 a.u.] exhibited good data quality, including high contributions from the ROI and low rates of pixel saturation. This dynamic range was further evaluated for robustness with different exposure times and particle concentrations. Understanding these relationships was necessary to make reliable, quantitative comparisons across clinical samples of unknown disease states.

**3.2.4 Fluorescence intensity increased linearly with exposure time.** Fluorescent polystyrene NPs were collected *via* DEP to characterize quantitative trends in fluorescence intensity and to determine the appropriate concentration of NPs to use as an internal standard in later experiments. Fluorescence intensity was plotted against exposure time for three concentrations of fluorescent polystyrene NPs spiked into healthy human plasma ( $0.52, 1.6, 4.7 \times 10^{10}$  beads per mL; Fig. 3a). Simple linear regressions were performed on the data in each contour. Coefficients of determination indicated a linear relationship between exposure time and fluorescence intensity over the usable dynamic range.

The observed relationship between fluorescence intensity and exposure time was consistent with how exposure time scales distributions of pixel intensities. Both the ROI and BG should scale by the same factor,  $c$ , for a  $c$ -fold increase in exposure time. The mean and standard deviation of the distribution of BG pixels should also increase by a factor of  $c$ . The noise threshold should increase by a factor of  $c$  as well (noise threshold = BG mean +  $3 \times$  BG std). The factor  $c$  should propagate through the remainder of the calculation to scale the final fluorescence intensity value, assuming the intensity value is within the dynamic range. Low contributions from the ROI and high pixel saturation outside the usable dynamic range suggested that limitations of the camera caused the ROI and BG pixel distributions to overlap or saturate (Fig. S3<sup>†</sup>), adversely affecting linearity with exposure time.

Similar trends were observed in fluorescence intensity and exposure time for EVs, which were labeled with anti-CD9-AF488 prior to isolation *via* DEP (Fig. 3c). Individual data represent the average of the sample means of fluorescence intensity of usable, noise-subtracted electrodes (one image per replicate; error bars show one standard deviation above and below the mean fluorescence intensity). We wanted to

confirm that signal from the internal standard in the DAPI fluorescence channel would not affect intensity values from labeled EVs in the adjacent EGFP channel. Control experiments confirmed that fluorescence from the internal standard was undetectable in the EGFP channel. Fluorescence levels from immunolabeled EVs through the DAPI channel were less than 1.5% of levels through the EGFP channel (data not shown). Together, these data indicate minimal spectral bleed through in adjacent DAPI and EGFP filter sets for the fluorescent labels used in these experiments.

Linear regressions were performed on fluorescence intensities within the dynamic range for separate contours of EV concentration. Best-fit lines were plotted through data within the dynamic range. All contours exhibited a high degree of linearity, suggesting that the presence of the internal standard had no effect on the relationship between fluorescence intensity and exposure time; however, the size of error bars in technical triplicate data suggested that non-physiological differences in collection efficiency across individual microfluidic chambers might adversely affect linearity. Intensities were adjusted later using the internal standard to account for collection efficiency, reducing variability in biomarker levels.

Fluorescence intensities above 2000 a.u. were not reliably quantitative due to pixel saturation. To obtain quantitative fluorescence values in situations with high pixel saturation, the acquisition exposure time could be reduced by a factor of  $c$  to shift the pixel distribution to lower values within limits of the photodetector in the camera. If quantification of the new image yielded a fluorescence intensity within the dynamic range and minimal pixel saturation, multiplying the fluorescence intensity by a factor  $c$  would yield a better estimate of the true fluorescence level than the original image acquired at a higher exposure. Therefore, linearity with exposure time can be exploited to expand the upper limit of the dynamic range.

**3.2.5 Fluorescence intensity increased linearly with particle concentration.** We characterized the relationship between fluorescence intensity and the concentration of fluorescent particles in the plasma samples and found that it was linear over the dynamic range (Fig. 3b). Linear fits were applied to fluorescence intensity values plotted against fluorescent particle concentration as three contours of exposure time (0.1, 0.2, 0.5 s). The physical presence of the internal standard did not prohibit observations of a linear relationship between fluorescence intensity and EV concentration for three contours of exposure time (0.5, 1.0, 2.0 s; Fig. 3d). Linear relationships between fluorescence intensity and particle concentration were anticipated over the usable dynamic range and consistent with other findings in the literature.

### 3.3 Characterization of the internal standard

A critical component of standardized fluorescence quantification is minimizing chip-to-chip variability in



collection efficiency. Our technique for minimizing variability across technical replicates was to use an internal standard consisting of a known concentration of fluorescent polystyrene NPs, which we spiked into biological samples. DEP forces collected the polystyrene NPs and the biological target particles simultaneously. The polystyrene NPs were selected to fluoresce at different wavelengths than the reporters used to label biological targets.

Adjusting fluorescence levels of labeled biomarkers to levels of the internal standard accounted for non-physiological differences in intensity. A chip with a low collection efficiency would isolate fewer polystyrene NPs and fewer biomarkers compared to a chip with high collection efficiency. Without the internal standard, we cannot be sure if a difference in biomarker fluorescence is due to a physiological difference in biomarker concentration, a difference in collection efficiencies across chips, or a combined effect. The internal standard enables us to adjust biomarker levels to minimize the impact of collection efficiency.

**3.3.1 Colocalization analysis confirms simultaneous collection of EVs and polystyrene NPs.** An analysis was performed using the Image J2 Coloc 2 plugin on individual electrodes within the array to determine the degree to which the polystyrene NPs colocalized with the EVs around the electrode edge. The average Pearson's *R* value (no threshold) for the polystyrene NPs (in red) and the CD9-labeled EVs (in green) was  $0.75 \pm 0.03$  (mean  $\pm$  standard deviation,  $n = 10$ ). This indicates a strong positive spatial correlation between the polystyrene NPs and the EVs as shown in yellow in Fig. 4e and f. This analysis shows that the DEP force acts similarly on both the polystyrene NPs and the EVs, making the NPs an appropriate internal standard for the EVs.

**3.3.2 Internal standard: linearity of fluorescence intensity with exposure time.** Adjusting intensities of immunofluorescently labeled EVs for collection efficiency using the internal standard did not affect the linear relationship between fluorescence intensity and exposure time. Comparisons of panels c and e in Fig. 3 highlighted that coefficients of determination for linear fits did not change after adjusting for collection efficiency.

**3.3.3 Internal standard: linearity of fluorescence intensity with concentration.** Adjusting intensities of immunofluorescently labeled EVs for collection efficiency using the internal standard improved the linear relationship between fluorescence intensity and EV concentration. Comparisons of panels d and f in Fig. 3 demonstrated that coefficients of determination for linear fits increased from approximately 0.96 to 0.99 for all contours of exposure time (0.5, 1.0, 2.0 s) after adjusting for collection efficiency.

**3.3.4 Internal standard reduced variability in technical replicates.** To determine how differences in collection efficiency affected biomarker levels, coefficients of variation (CVs) were calculated for technical triplicates of immunofluorescently labeled EVs. CVs were also calculated for intensities that had been adjusted for collection efficiency using the internal standard (Fig. 5). All intensity values used

to calculate CVs were within the dynamic range. Adjusted intensities exhibited lower CVs at all detectable concentrations of EVs, confirming that the internal standard partially corrected for variability in technical replicates.

Taken together with data shown in Fig. 3f, the internal standard effectively reduced the variability in technical replicates while improving the linear relationship between EV concentration and fluorescence intensity. Furthermore, the presence of the internal standard did not affect the linear relationship between fluorescence intensity and exposure time (Fig. 3e). Therefore, the internal standard was shown to be beneficial for quantifying biomarkers collected with DEP chip technology.

## Conclusion

We designed an algorithm to quantify the fluorescence intensity of labeled NPs collected in predictable locations within a microfluidic device. We demonstrated the utility of this algorithm by using an electrode microarray chip to collect EVs and polystyrene NPs from blood plasma *via* DEP forces. Quantification was achieved by comparing pixel intensity values in regions of high-field DEP, where the particles preferentially accumulated, to values at adjacent regions of low-field DEP, which served as BG. We automated the entire process including removal of optical artifacts, the determination of fluorescence intensity, and the creation of reports. Automation helped standardize analysis by minimizing user bias and improving throughput. We then identified a usable dynamic range in fluorescence intensity values. We established the lower limit of the usable dynamic range by correlating fluorescence intensity with the predicted location of the source of fluorescence. Correlations between fluorescence intensity and the percentage of saturated pixels defined the upper limit of the usable dynamic range. As anticipated, we observed linear relationships between fluorescence intensity and exposure time at multiple concentrations of particles within the dynamic range. We also demonstrated that fluorescence intensity increased linearly with particle concentration at multiple exposure times within the dynamic range. By tailoring the digital mask to encompass regions of collection, the algorithm described in this paper can be translated to other fluorescence-based platforms for liquid biopsy.

We also developed an internal standard to correct for chip-to-chip variability in collection efficiency. Spiking a known concentration of fluorescent polystyrene NPs into biological samples enabled us to partially correct for variability in fluorescence intensity across technical replicates. Adjusting for collection efficiency did not change linear trends between fluorescence intensity and exposure time; however, use of the internal standard improved the linearity of fit for fluorescence intensity and biomarker concentration. Use of the internal standard reduced the measured variability in technical replicates by correcting for differences in collection efficiency across DEP chips. The



internal standard will be important for comparing biomarker levels between clinical patient samples of unknown disease states. Controlling for non-physiological variability in biomarker levels is especially critical for the detection of early stage cancer, which often exhibits low circulating concentrations of prognostic biomarkers.

## Author contributions

K. T. Gustafson designed the algorithm, harvested EVs from cell culture media, performed experiments, acquired images, analyzed data, assembled figures, and wrote the manuscript. K. Huynh harvested EVs from cell culture media, performed experiments, acquired images and electron micrographs, and analyzed data. D. Heineck provided feedback during algorithm design and optimization, and obtained data from simulations. J. Bueno and A. Modestino performed experiments, acquired images, and provided feedback during algorithm design and optimization. S. Kim acquired electron micrographs. A. Gower and R. Armstrong purified, concentrated, and characterized EVs from cell culture media. C. E. Schutt performed colocalization analyses of EVs and fluorescent NPs collected simultaneously using DEP. S. Ibsen oversaw all work, helping to create the algorithm, design experiments, analyze data, assemble figures, and write the manuscript.

## Conflicts of interest

D. Heineck is an employee of Biological Dynamics.

## Acknowledgements

This project was supported by funding (CEDAR Project Full4960219) from the Cancer Early Detection Advanced Research Center at Oregon Health & Science University's Knight Cancer Institute. Human plasma specimens were provided by the Brenden-Colson Center for Pancreatic Care, the Oregon Pancreas Tissue Registry, and the OHSU Knight Cancer Institute CEDAR Center Repository. Electron microscopy was performed at the Multiscale Microscopy Core, a member of the OHSU University Shared Resource Cores. K. T. Gustafson would like to thank the Achievement Rewards for College Scientists (ARCS) Foundation Oregon for their financial support.

## References

- 1 N. Festjens, T. V. Berghe and P. Vandenabeele, *Biochim Biophys Acta Bioenerg*, 2006, **1757**, 1371–1387.
- 2 M. An, I. Lohse, Z. Tan, J. Zhu, J. Wu, H. Kurapati, M. A. Morgan, T. S. Lawrence, K. C. Cuneo and D. M. Lubman, *J. Proteome Res.*, 2017, **16**, 1763–1772.
- 3 M. Ilies, P. K. Sappa, C. A. Iuga, F. Loghin, M. G. Salazar, F. U. Weiss, G. Beyer, M. M. Lerch, U. Völker and J. Mayerle, *Clin. Chim. Acta*, 2018, **477**, 127–134.
- 4 T. Yoneyama, S. Ohtsuki, K. Honda, M. Kobayashi, M. Iwasaki, Y. Uchida, T. Okusaka, S. Nakamori, M. Shimahara and T. Ueno, *PLoS One*, 2016, **11**(8), e0161009.
- 5 H. Schwarzenbach, D. S. Hoon and K. Pantel, *Nat. Rev. Cancer*, 2011, **11**, 426–437.
- 6 D. Duijvesz, T. Luider, C. H. Bangma and G. Jenster, *Eur. Urol.*, 2011, **59**, 823–831.
- 7 D. D. Taylor and S. Shah, *Methods*, 2015, **87**, 3–10.
- 8 A. V. Vlassov, S. Magdaleno, R. Setterquist and R. Conrad, *Biochim Biophys Acta Gen Subj*, 2012, **1820**, 940–948.
- 9 L. Muller, C.-S. Hong, D. B. Stolz, S. C. Watkins and T. L. Whiteside, *J. Immunol. Methods*, 2014, **411**, 55–65.
- 10 H. Kalra, C. G. Adda, M. Liem, C. S. Ang, A. Mechler, R. J. Simpson, M. D. Hulett and S. Mathivanan, *Proteomics*, 2013, **13**, 3354–3364.
- 11 R. J. Lobb, M. Becker, S. Wen Wen, C. S. Wong, A. P. Wiegman, A. Leimgruber and A. Möller, *J. Extracell. Vesicles*, 2015, **4**, 27031.
- 12 D. D. Taylor, W. Zacharias and C. Gercel-Taylor, in *Serum/plasma proteomics*, Springer, 2011, pp. 235–246.
- 13 A. E. Frampton, M. M. Prado, E. López-Jiménez, A. B. Fajardo-Puerta, Z. A. Jawad, P. Lawton, E. Giovannetti, N. A. Habib, L. Castellano and J. Stebbing, *Oncotarget*, 2018, **9**, 19006.
- 14 S. D. Ibsen, J. Wright, J. M. Lewis, S. Kim, S.-Y. Ko, J. Ong, S. Manouchehri, A. Vyas, J. Akers and C. C. Chen, *ACS Nano*, 2017, **11**, 6641–6651.
- 15 J. M. Lewis, A. D. Vyas, Y. Qiu, K. S. Messer, R. White and M. J. Heller, *ACS Nano*, 2018, **12**, 3311–3320.
- 16 S. Ibsen, A. Sonnenberg, C. Schutt, R. Mukthavaram, Y. Yeh, I. Ortac, S. Manouchehri, S. Kesari, S. Esener and M. J. Heller, *Small*, 2015, **11**, 5088–5096.
- 17 A. Castellanos, A. Ramos, A. Gonzalez, N. G. Green and H. Morgan, *J. Phys. D: Appl. Phys.*, 2003, **36**, 2584.
- 18 Z. W. Kendrick, M. A. Firpo, R. C. Repko, C. L. Scaife, D. G. Adler, K. M. Boucher and S. J. Mulvihill, *HPB*, 2014, **16**, 670–676.
- 19 S. S. Hori and S. S. Gambhir, *Sci. Transl. Med.*, 2011, **3**, 109ra116.
- 20 S. S. Hori, A. M. Lutz, R. Paulmurugan and S. S. Gambhir, *Cancer Res.*, 2017, **77**, 2570–2584.
- 21 A. R. Yale, J. L. Nourse, K. R. Lee, S. N. Ahmed, J. Arulmoli, A. Y. Jiang, L. P. McDonnell, G. A. Botten, A. P. Lee and E. S. Monuki, *Stem Cell Rep.*, 2018, **11**, 869–882.
- 22 N. Alinezhadbalalami, T. A. Douglas, N. Balani, S. S. Verbridge and R. V. Davalos, *Electrophoresis*, 2019, **40**, 2592–2600.
- 23 M. Elitas, Y. Yildizhan, M. Islam, R. Martinez-Duarte and D. Ozkazanc, *Electrophoresis*, 2019, **40**, 315–321.
- 24 A. Sonnenberg, J. Y. Marciniak, R. Krishnan and M. J. Heller, *Electrophoresis*, 2012, **33**, 2482–2490.
- 25 E. A. Henslee, M. B. Sano, A. D. Rojas, E. M. Schmelz and R. V. Davalos, *Electrophoresis*, 2011, **32**, 2523–2529.
- 26 T. A. Douglas, J. Cemazar, N. Balani, D. C. Sweeney, E. M. Schmelz and R. V. Davalos, *Electrophoresis*, 2017, **38**, 1507–1514.
- 27 Y. Qin, L. Wu, T. Schneider, G. S. Yen, J. Wang, S. Xu, M. Li, A. L. Paguirigan, J. L. Smith and J. P. Radich, *Angew. Chem., Int. Ed.*, 2018, **57**, 11378–11383.
- 28 C. V. Crowther, S. H. Hilton, L. Kemp and M. A. Hayes, *Anal. Chim. Acta*, 2019, **1068**, 41–51.



- 29 I. H. Su, W. C. Ko, C. H. Shih, F. H. Yeh, Y. N. Sun, J. C. Chen, P. L. Chen and H. C. Chang, *Anal. Chem.*, 2017, **89**, 4635–4641.
- 30 J. Ding, R. M. Lawrence, P. V. Jones, B. G. Hogue and M. A. Hayes, *Analyst*, 2016, **141**, 1997–2008.
- 31 E. Iswardy, T.-C. Tsai, I.-F. Cheng, T.-C. Ho, G. C. Perng and H.-C. Chang, *Biosens. Bioelectron.*, 2017, **95**, 174–180.
- 32 D. V. Polniak, E. Goodrich, N. Hill and B. H. Lapizco-Encinas, *J. Chromatogr. A*, 2018, **1545**, 84–92.
- 33 V. H. Perez-Gonzalez, R. C. Gallo-Villanueva, B. Cardenas-Benitez, S. O. Martinez-Chapa and B. H. Lapizco-Encinas, *Anal. Chem.*, 2018, **90**, 4310–4315.
- 34 A. Floris, S. Staal, S. Lenk, E. Staijen, D. Kohlheyer, J. Eijkel and A. van den Berg, *Lab Chip*, 2010, **10**, 1799–1806.
- 35 C. Hale and J. Darabi, *Biomicrofluidics*, 2014, **8**, 044118.
- 36 B. D. Plouffe, M. Mahalanabis, L. H. Lewis, C. M. Klapperich and S. K. Murthy, *Anal. Chem.*, 2012, **84**, 1336–1344.
- 37 K. Olofsson, B. Hammarstrom and M. Wiklund, *Lab Chip*, 2020, **20**, 1981–1990.
- 38 A. Urbansky, F. Olm, S. Scheduling, T. Laurell and A. Lenshof, *Lab Chip*, 2019, **19**, 1406–1416.
- 39 Z. Ramshani, C. Zhang, K. Richards, L. Chen, G. Xu, B. L. Stiles, R. Hill, S. Senapati, D. B. Go and H. C. Chang, *Commun. Biol.*, 2019, **2**, 189.
- 40 M. He, J. Crow, M. Roth, Y. Zeng and A. K. Godwin, *Lab Chip*, 2014, **14**, 3773–3780.
- 41 S. S. Kanwar, C. J. Dunlay, D. M. Simeone and S. Nagraath, *Lab Chip*, 2014, **14**, 1891–1900.
- 42 M. S. Loeian, S. Mehdi Aghaei, F. Farhadi, V. Rai, H. W. Yang, M. D. Johnson, F. Aqil, M. Mandadi, S. N. Rai and B. Panchapakesan, *Lab Chip*, 2019, **19**, 1899–1915.
- 43 The MathWorks™, Inc. MATLAB®. Version 9.3.0.713579 (2017b), Natick, MA, 2017.
- 44 The MathWorks™, Inc. Image Processing Toolbox (Version 10.1), Natick, MA, 2017, <https://www.mathworks.com/help/images>.
- 45 The MathWorks™, Inc. MATLAB® Answers, Natick, MA, <https://www.mathworks.com/matlabcentral/answers/index>.

